Design of novel transition-metal-doped C_4N_4 as highly effective electrocatalysts for nitrogen fixation with a new intrinsic descriptor

Cheng He [a], Jianglong Ma [a], Yibo Wu [a], Wenxue Zhang [b,*]

[a] *State Key Laboratory for Mechanical Behavior of Materials, School of Materials Science and Engineering, Xi'an Jiaotong University, Xi'an 710049, Shaanxi, China*
[b] *School of Materials Science and Engineering, Chang'an University, Xi'an 710064, Shaanxi, China*

ARTICLE INFO

ABSTRACT

Electrocatalytic nitrogen reduction reaction (NRR) is an efficient and green way to produce ammonia, which offers an alternative option to the conventional Haber-Bosch process. Unfortunately, the large-scale industrial application of NRR processes is still hindered by poor Faraday efficiency and high overpotential, which need to be overcome urgently. Herein, combined with density functional theory and particle swarm optimization algorithm for the nitrogen carbide monolayer structural search (C_mN_{8-m}, m = 1–7), the surprising discovery is that single transition metal-atom-doped C_4N_4 monolayers (TM@C_4N_4) could effectively accelerate nitrogen reduction reaction. TM@C_4N_4 (TM = 29 transition metals) as single-atom catalysts are evaluated via traditional multi-step screening method, and their structures, NRR activity, selectivity and solvation effect are investigated to evaluate their NRR performance. Through the screening steps, W@C_4N_4 possesses the highest activity for NRR with a very low limiting potential of -0.29 V. Moreover, an intrinsic descriptor φ is proposed with machine learning, which shortens the screening process and provides a new idea for finding efficient SACs. This work not only offers promising catalysts W@C_4N_4 for NRR process but also offers a new intrinsic and universal descriptor φ.
© 2023 Science Press and Dalian Institute of Chemical Physics, Chinese Academy of Sciences. Published by ELSEVIER B.V. and Science Press. All rights reserved.

1. Introduction

The energy crisis and the greenhouse effect threaten the rapid development of human society [1]. Ammonia has attracted much attention due to its high hydrogen density (17.8 wt%) and easy liquefaction (8 atm), as green energy to ease the energy crisis and achieve carbon neutrality [2–5]. Moreover, ammonia is an essential industrial raw materials in fiber synthesis, medicine manufacturing, agriculture and other fields [6–8]. However, the traditional nitrogen manufacturing method, the Haber − Bosch process needs to be carried out under high temperature (700 K) and high pressure (100 bar) [9]. It consumes 2% of humanity's annual energy consumption and releases huge carbon dioxide [10,11]. It is urgent to find an environmentally friendly method for producing ammonia. What's exciting is that the electrocatalytic nitrogen reduction reaction (NRR) is currently the most prospective replacement of the Haber-Bosch process [12,13]. The key to NRR is to weaken the N≡N bonds in N_2 molecules through efficient catalysts, in order

to achieve ammonia synthesis at room temperature and pressure [14]. Therefore, it is imperative to develop new and efficient NRR catalysts.

Single-atom catalysts (SACs), is defined as a substrate loaded with uniformly dispersed single metal atoms [15,16]. Such catalysts have attracted a lot of attention due to their excellent advantages: (1) Maximize the metal utilization rate and save the cost of precious metals [17]. (2) The uniform dispersion of metals provides a large number of active sites [18]. (3) Transition metal d orbitals possess abundant valence electrons and empty orbitals simultaneously, which can produce strong electronic interaction with reactants [19–21]. In addition, the determined coordination of the active site makes the reaction highly selective and helps to elucidate the catalytic mechanism [22–24]. Due to these advantages, SACs have made a series of satisfying achievements in NRR very recently [5,25–31]. However, the current single atom catalyst has not achieved industrial production, and it is necessary to find an appropriate substrate to achieve efficient SACs. Therefore, many 2D materials are researched as substrates for their large specific surface areas and specific electronic properties [32–35]. Zhai *et al.* screened the electrocatalytic performance of TM@MoS_2 and Re supported on MoS_2 get the best activity of NRR with the limiting

---

* Corresponding author.
E-mail address: wxzhang@chd.edu.cn (W. Zhang).

potential of −0.43 V [36]. Liu *et al.* designed a series of transition single metal atom anchored on the black phosphorene and calculated their performance for NRR process. The W@BP has the best performance and has a limiting potential of −0.42 V [37]. However, the preparation materials of MoS_2 and black phosphorene are expensive and scarce. Due to the widely distributed of carbon source materials, carbon based materials such as graphene [38,39], N-doped graphene [40,41], g-C_3N_4 [42,43] and g-C_2N [44,45] have been widely explored as substrates of SACs, which is due to their cheap constituent materials and the simple synthesis methods. Herein, the particle swarm optimization (PSO) algorithm is used to search the different nitrogen carbide monolayer structures (C_mN_{8-m}, m = 1–7) [46]. Among them, the C_4N_4 shows the best structural stability due to its lowest formation energy. In summary, the SACs composed of C_4N_4 possess all the advantages mentioned above, and it is the most stable material among the predicted nitrogen carbide monolayer structures (C_mN_{8-m}, m = 1–7). For these reasons, C_4N_4 is selected as the substrate for SACs in subsequent research.

Herein, C_4N_4 is doped with 29 kinds of transition metal elements to construct a series of TM@C_4N_4. Then, stability, adsorption free energy of N_2, NRR process pathway and selectivity are investigated to screen the promising catalysts by using density functional theory (DFT) calculation. Thereafter, the influence of implicit solvation model is considered, W@C_4N_4 and Re@C_4N_4 obtain the best performance. Through the analysis of electronic properties and electron transfer for W@C_4N_4 and Re@C_4N_4, the origin of NRR activity is obtained, which provides theoretical guidance for the research and development of new NRR catalysts. Moreover, in order to greatly speed up the screening process of finding efficient NRR catalysts, the descriptor φ composed of intrinsic properties of TM atoms is identified by machine learning method of Sure Independence Screening and Sparsifying Operator (SISSO) [47]. This work demonstrates that W@C_4N_4 and Re@C_4N_4 are excellent catalysts of NRR and provide a promising guidance for electrocatalytic NRR.

2. Theoretical approach

The different nitrogen carbide monolayer structures (C_mN_{8-m}, m = 1–7) are searched with the particle swarm optimization (PSO) algorithm, which is implemented by the particle swarm optimization (CALYPSO) code in crystal structure analysis [46]. All of the first-principle spin polarization computations are obtained in the Vienna ab initio Simulation Package (VASP) [48,49]. In order to demonstrate the electron exchange correlation functional, the Perdew − Burke − Ernzerhof (PBE) function as advanced by generalized gradient approximation (GGA) is used [50,51]. To describe the ion–electron interaction, the projector augmented wave (PAW) potential is employed [52]. The cut off energy of 400 eV is set in the process of structural optimization, the $4 \times 4 \times 1$ Monkhorst–Pack k-point meshes are used to sample the Brillouin region. The criterion of convergence for energy is 10^{-5} eV, and for force, it is 0.02 eV/Å. The long-range van der Waals interaction is determined using the Grimme's DFT-D3 scheme [53], and a vacuum space of 20 Å is added in vertical direction which is enough to eliminate the interactions between periodic layers. The NVT ensemble and Andersen thermostat is used to perform molecular dynamics simulations. The charge transfer between each part of catalysts is computed by Bader analysis. The solvation effects are under consideration, and the VASPsol is used to implement an implicit solvation model, in which the dielectric constant was set to 78.45 [54,55]. The package of SISSO was used to obtain simple intrinsic descriptor φ, which can forecast the activity of SACs for NRR process.

The formation energy of C_mN_{8-m} is defined as follows:

$$E_f = E_{C_mN_{8-m}} - m\mu_C - (8 - m)\mu_N \tag{1}$$

Where $E_{C_mN_{8-m}}$ represents the total energy of the C_mN_{8-m}. The m and 8-m represent the number of carbon and nitrogen atoms in the unit cell of C_mN_{8-m}, respectively. The μ_C and μ_N correspond to the chemical potentials of carbon and nitrogen, which are defined as the total energy of graphene per carbon and one-half of the total energy of N_2 molecule, respectively.

The binding energy between the TM atom and C_4N_4 is defined as follows:

$$E_b = E_{TM@C_4N_4} - E_{substrate} - E_{TM} \tag{2}$$

Where $E_{TM@C_4N_4}$ and $E_{substrate}$ represent the energy of the TM@C_4N_4 and the bare C_4N_4 with a vacancy that has not been doped TM atom. The E_{TM} represents the total energy of single transition metal atom.

The changes of Gibbs free energy (ΔG) of each NRR basic step are defined as follows:

$$\Delta G = \Delta E + \Delta E_{ZPE} - T\Delta S + \Delta G_{PH} + \Delta G_U \tag{3}$$

Where ΔE represents the difference of electronic energy between the product and reactant, which was directly computed from the DFT calculation. ΔE_{ZPE} and ΔS are the variation in zero point energies and entropy change at 298.15 K. ΔG_{PH} is computed by $\Delta G_{PH} = k_B T \times pH \times \ln10$, which is the correction of free energy for pH, the pH is assigned the value of zero in this research, and k_B is the Boltzmann constant respectively. The ΔG_U represents the contribution of free energy, which originate from the applied electrode potential (U).

Thus, the changes of Gibbs free energy (ΔG) lead to the N_2 adsorption free energies for TM@C_4N_4, which are defined as follows:

$$\Delta G_{*N_2} = G_{*N_2} - G_* - G_{N_2} \tag{4}$$

Where G_{*N_2} represents the total Gibbs free energy of TM@C_4N_4, which has adsorbed nitrogen molecule. The G_* represents the Gibbs free energy of separate TM@C_4N_4, and G_{N_2} represents the Gibbs free energy of isolated nitrogen molecule.

The limiting potential (U_L) is defined as follows:

$$U_L = -\Delta G_{max}/e \tag{5}$$

Where ΔG_{max} represents the maximum change of free energy among each elementary step alone the lowest-energy pathway, which is called potential-determining step (PDS) in the NRR process.

3. Results and discussion

3.1. Structure and stability of TM@C_4N_4

Several stoichiometric (C_mN_{8-m}, m = 1–7) carbonized nitrogen monolayers are obtained using the CALYPSO code. In order to get the most stable substrate, their relative formation energies are calculated as shown in Fig. 1(a), and the C_4N_4 possess the best performance due to its lowest relative formation energy of −3.60 eV. The C_4N_4 monolayer has a puckered structure which is formed of C atoms and N atoms. The (2×2) supercell of C_4N_4 is constructed with the lattice a = 7.17 Å, b = 12.2 Å in this work. The 29 kinds of transition metals are considered by doping the C_4N_4 supercell, and the geometric structures of TM@C_4N_4 and pristine C_4N_4 are shown in Fig. 1(b) and Fig. S1. Most of the optimized structures of TM@C_4N_4 are folded, and the metal atoms of partial TM@C_4N_4 have bulged from the C_4N_4 plane. More details are presented in Fig. S1. In the NRR process, one of the indispensable performances
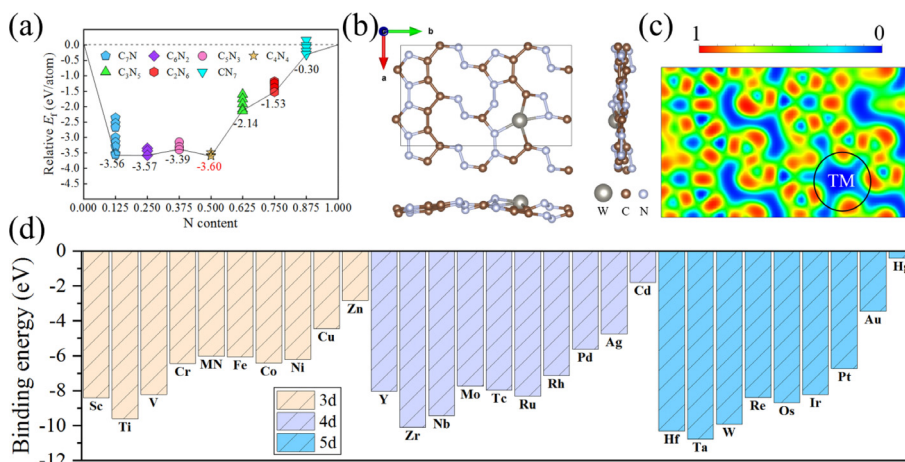
Fig. 1. (a) Relative formation energies of nitrogen carbide monolayer structures (C_mN_{8-m}, m = 1–7). (b) The structures of W@C_4N_4. (c) The ELF map of W@C_4N_4. The positions of the metal atoms have been marked in the figure. (d) Calculated binding energy E_b of the TM atoms in the TM@C_4N_4 SACs.

of catalysts is to maintain structural stability and their bonding characters are computed by the electron localization function (ELF) as shown in Fig. 1(c) and Fig. S2. Generally speaking, a large ELF value describes a covalent bond type between atoms and a smaller ELF value corresponds the ionic bond. It could be found that the ELF value between TM atom and coordination atoms is close to the max value, which means the strong covalent is formed, the metal atoms are tightly doped to the substrate. In order to obtain the strength of binding between the substrate and the metal atoms, the E_b between the TM atoms and C_4N_4 are calculated to illustrate whether metal atoms tend to stick to the substrate. In Fig. 1(d), all of binding energies are negative, and Ta@C_4N_4 gets the most negative binding energy (-10.7 eV). The binding energies of most elements are more negative than −6 eV. Here, the binding energies of TM@C_4N_4 are compared with that of other common SACs such as TM@g-C_3N_4 [43], TM@g-CN [56], TM@MoS_2 [36] and TM@GY [57]. The most binding energies of TM@g-C_3N_4, TM@g-CN, TM@MoS_2 and TM@GY are more positive than −6 V, and Sc@g-C_3N_4 get the most negative binding energy (-7.50 eV), which is more positive than Sc@C_4N_4 (-8.41 eV). Therefore, the metal atoms in TM@C_4N_4 are very tightly doped to the substrate, and TM@C_4N_4 has extremely high structural stability.

3.2. N_2 adsorption and activation

The adsorption and activation of the N_2 molecule are very critical steps in NRR, which is due to a high requirement of energy for breaking the N≡N. Fortunately, the TM atoms can effectively activate the N_2 molecule by the mechanism called "donation and backdonation" [58]. As shown in Fig. 2(a), the TM atoms have the occupied d orbitals filled with valence electrons and empty d orbitals simultaneously, and thus the lone-pairs electrons of N_2 molecule are captured by empty d orbitals of TM atoms. Meanwhile, the π^* antibonding orbitals of N≡N bond can receive the backdonation electrons from the occupied orbitals of TM atoms, which weaken the bond strength of N_2 molecule. Hence, the N_2 molecule become activated, which is a prerequisite for NRR to proceed. Then the ΔG_{*N_2} and the changes in N≡N bond length during adsorption process are analyzed for revealing N_2 activation. In particular, for N_2 molecule, two adsorption configurations which are called side-on configuration and end-on configuration constantly occur on the metal atoms. In the end-on configuration, the distances between the two nitrogen atoms and the metal atoms are very different, and only the closer atom build bonds with the metal atom. Regarding side-on configuration, both nitrogen atoms are adjacent to and

bonded to the metal atom. For 29 TM@C_4N_4, 58 different adsorption configurations including side-on and end-on configuration are calculated. The structural stabilities of Pd@C_4N_4, Ag@C_4N_4 and Hg@C_4N_4 are broken, and N_2 is not effectively captured for TM@C_4N_4 (TM = Co, Ni, Cu, Zn, Tc, Rh, Cd, Re, Os, Ir, Pt, Au) in side-on configuration and TM@C_4N_4 (TM = Mn, Cu, Zn, Rh, Cd, Ir, Pt, Au) in end-on configuration. The configurational transformation appears in structure optimization for TM@C_4N_4 (TM = Sc, Cr, Mn, Fe, Y, Ru), in which their side-on configuration is transformed into end-on configuration, which indicates that the TM@C_4N_4 (TM = Sc, Cr, Mn, Fe, Y, Ru) is prefer end-on configuration over side-on configuration. That is because the 4-coordination structure of metal atoms leads to their outer electron orbitals being nearly saturated, and it is very difficult for these metal atoms to bond with two nitrogen atoms simultaneously. So, the rest TM@C_4N_4 (TM = Ti, V, Zr, Nb, Mo, Hf, Ta, W) in side-on configuration and TM@C_4N_4 (TM = Sc, Ti, V, Cr, Fe, Co, Ni, Y, Zr, Nb, Mo, Tc, Ru, Hf, Ta, W, Re, Os) are further studied. The adsorption free energies are computed and the bond length of N_2 molecule is researched for revealing of N_2 activation. The adsorption free energies of Ti@C_4N_4, V@C_4N_4 in side-on configurations and Cr@C_4N_4, Co@C_4N_4 in end-on configurations are 0.03 eV, 0.15 eV, 0.17 eV and 0.15 eV as shown in Fig. 2(b), which are removed consideration due to their positive adsorption free energies. In all adsorption configurations, N≡N bonds are activated according to the bond length is longer than the pristine N_2 molecule (1.117 Å), and the bond length for side-on configurations are always much longer than that for the end-on configuration. The longest N≡N bond length (1.21 Å) is the W@C_4N_4 (side-on), and the shortest N≡N bond length in side-on configurations is 1.13 Å, which is close to the longest end-on configuration of Ta@C_4N_4 (1.15 Å). In the side-on configurations, both nitrogen atoms are directly receiving feedback electrons from the metal atom, leading to a greater weakening for N≡N bond. However, in terms of adsorption free energies, the end-on configurations have lower values such as Zr@C_4N_4, Nb@C_4N_4, Mo@C_4N_4, Hf@C_4N_4, Ta@C_4N_4 and W@C_4N_4. Therefore, end-on configurations are easily constituted due to lower adsorption free energy and higher structural stability. Hence, only the TM@C_4N_4 (Sc, Ti, V, Fe, Ni, Y, Zr, Nb, Mo, Tc, Ru, Hf, Ta, W, Re, Os) in end-on configuration is focused in the further discussion.

3.3. Reaction mechanism and selectivity for NRR

The NRR process is a six-electron reaction (N_2 + 6H$^+$ + 6e$^-$ = 2NH$_3$). According to very recent research, the first step of
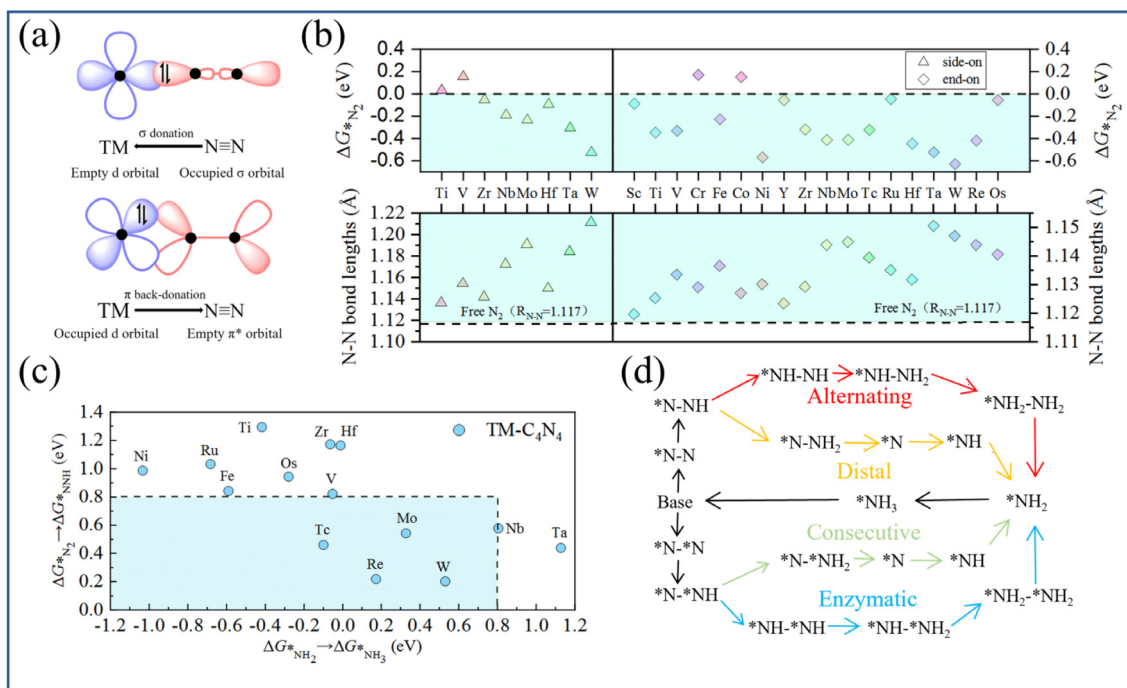
Fig. 2. (a) The "donation and backdonation" mechanism. (b) The N_2 adsorption free energy (ΔG_{*N_2}) and the N≡N bond length after adsorption of TM@C$_4$N$_4$. (c) The Gibbs free energy changes (ΔG) of the first hydrogenation step and the last hydrogenation step of TM@C$_4$N$_4$. (d) The four common NRR pathways: alternating, distal, consecutive and enzymatic pathway.

hydrogenation reaction (*N_2 + H$^+$ + e$^-$ = *N_2H) and the last hydrogenation step (*NH_2 + H$^+$ + e$^-$ = *NH_3) get high probability to constitute the potential-determining step (PDS) with the maximum ΔG [59]. In particular, after the catalysts complete the NRR process to produce NH_3, NH_3 needs to be removed from the substrate. In acidic conditions, NH_3 can get further hydrogenation to form NH_4^+, and thus, there is no great obstacle in desorption of NH_3 on TM@C$_4$N$_4$ [60]. To obtain the best performance SACs among TM@C$_4$N$_4$ for NRR, the ΔG in the first and last hydrogenation steps are calculated. As shown in Fig. 2(c), the TM@C$_4$N$_4$ (TM = Tc, Mo, Re, W) are excluded because they satisfy the criteria of $\Delta G_{*N_2 \rightarrow *N_2H}$ < 0.8 eV and $\Delta G_{*NH_2 \rightarrow *NH_3}$ < 0.8 eV. The $\Delta G_{*N_2 \rightarrow *N_2H}$ of Tc@C$_4$N$_4$ (0.46 eV), Mo@C$_4$N$_4$ (0.54 eV) are larger than $\Delta G_{*NH_2 \rightarrow *NH_3}$ of them which indicates that their first hydrogenation step is more likely to be the PDS in all NRR steps. For W@C$_4$N$_4$, the $\Delta G_{*N_2 \rightarrow *N_2H}$ is 0.53 eV, which is much bigger than ΔG in the first hydrogenation. Therefore, for W@C$_4$N$_4$, the last hydrogenation step is more likely to be the PDS. It is worth mentioned that Re@C$_4$C$_4$ has the smallest value in $\Delta G_{*N_2 \rightarrow *N_2H}$ (0.22 eV) and $\Delta G_{*NH_2 \rightarrow *NH_3}$ (0.17 eV) simultaneously, and Tc is a radioactive element, which leads to its exclusion for being efficient NRR catalysts. Hence, the Mo@C$_4$N$_4$, W@C$_4$N$_4$ and Re@C$_4$N$_4$ are remaining for the further study.

The four possible reaction pathways in NRR process are studied for screening out the best catalyst with the highest NRR activity as shown in Fig. 2(d). There is no difference in the first two steps between the consecutive pathway and enzymatic pathway, and N_2 molecule builds bonds with the metal atom in side-on adsorption configuration. Then, one of the nitrogen atoms receives a pair of proton and electron, and forms an intermediate *N*NH, and the change in Gibbs free energy is almost the same in this step regardless of which nitrogen atom is hydrogenated. In consecutive pathway, the proton will keep attacking the nitrogen atom which is hydrogenated until the *N*NH$_3$ is formed, and the first NH_3 is released and the remaining nitrogen atom continues the hydrogenation process. In enzymatic pathway, the proton bond with

the nitrogen atom which has not been hydrogenated. The *NH*NH species is generated, then hydrogenation process alternates between the two nitrogen atoms until NH_3 is released from species *NH_2*NH_3, and *NH_2 species is left. After the last hydrogenation step, the whole NRR process is completed in enzymatic pathway. After the screening process above, only Mo@C$_4$N$_4$, W@C$_4$N$_4$ and Re@C$_4$N$_4$ are remaining, and all of them are end-on adsorption configurations.

The changes of Gibbs free energies along alternating pathway and distal pathway for Mo@C$_4$N$_4$, W@C$_4$N$_4$ and Re@C$_4$N$_4$ are calculated to get their limiting potentials (U_L). As shown in Fig. 3(a), for the Mo@C$_4$N$_4$ in a vacuum, the N_2 molecule was adsorbed on substrate with −0.41 eV adsorption free energy, indicating that this structure effectively traps nitrogen molecules. Then, the nitrogen atom on the remote side is hydrogenated to generate species *NNH. This step is accompanied by an increase with the ΔG of 0.54 eV, and it is PDS both in distal and alternating pathway. In distal pathway, the second hydrogenation step generates the species *NNH$_2$ from species *NNH with ΔG of −0.53 eV. Following, the next step which is also the third step proceeds, and the protons are continually trapped by the nitrogen atom at the far end, which results in the formation of *N species. The NH_3 is released by accomplishing the third hydrogenation step with the ΔG of −0.51 eV. Then hydrogenation process continues, the *NH, *NH_2 and *NH_3 are formed in next three hydrogenation steps by the ΔG of −0.65 eV, −0.24 eV and 0.33 eV. At this point, the entire 6-steps NRR reaction is completed in distal pathway. As shown in Fig. S3(a), in alternating pathway, the nitrogen molecule adsorption process and first hydrogenation step are the same as distal pathway. The difference is that in the second step, a pair of proton and electron is received by the nitrogen atom, which is closer to the metal atom, and the *NNH species are converted to the *NHNH species with ΔG of 0.11 eV, and then the second step performs with formation of *NHNH species and the ΔG of this step is −0.20 eV. The fourth step conducts in another nitrogen atom, and *NH_2NH$_2$ is formed with ΔG of 0.26 eV. After, for *NH_2NH$_2$ species, a pair
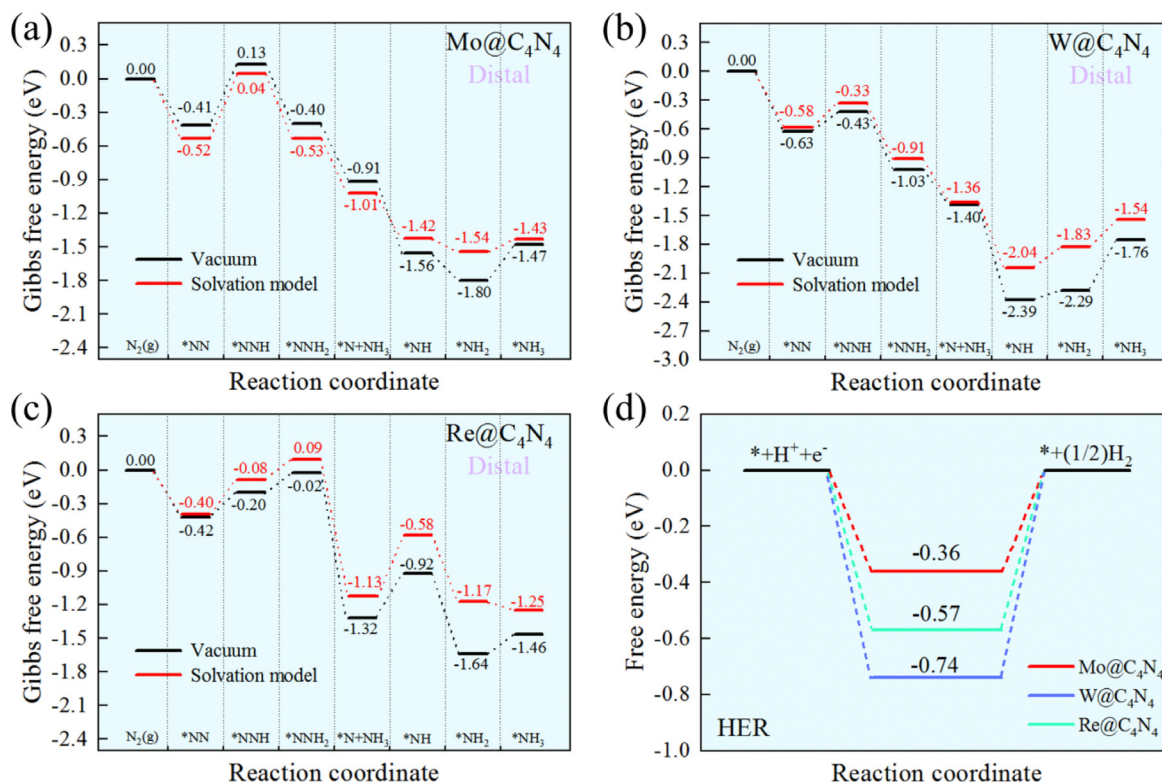
Fig. 3. (a-c) The Gibbs free energy diagrams for the distal pathway of NRR catalyzed by Mo@C$_4$N$_4$, W@C$_4$N$_4$ and Re@C$_4$N$_4$. (d) Schematic diagram of hydrogen evolution reaction on Mo@C$_4$N$_4$, W@C$_4$N4 and Re@C$_4$N$_4$.

of proton and electron is accepted and *NH$_2$ species are left on the substrate. Meanwhile, NH$_3$ species is released resulting in ΔG of −2.11 eV, and after the last step with ΔG of 0.33 eV, another NH$_3$ species is formed. In two different pathways, the first steps which act as potential-determining steps (PDS) both have the limiting potential (U_L) of −0.54 V. In distal pathway, the steps besides the first step and the last step are all exothermic reaction, which means these steps are thermodynamic spontaneous progression. In general, since the limiting potential and PDS are the same in two different pathways, the NRR process can occur in both paths for Mo@C$_4$N$_4$. Then the NRR pathway of W@C$_4$N$_4$ in vacuum is researched including distal and alternating pathways. Similar to Mo@C$_4$N$_4$, nitrogen is adsorbed on substrate in end-on configuration with the adsorption free energy of −0.63 eV as shown in Fig. 3(b), and the first step generates the *NNH species with an extremely low ΔG (0.20 eV). In distal pathway, followed by the second step, the *NNH species are converted to *NNH$_2$ species with ΔG of −0.60 eV. Next, three hydrogenation steps take place in sequence with ΔG of −0.37 eV, −0.99 eV and 0.10 eV. And the last hydrogenation step gets the most increase ΔG with 0.53 eV as the PDS for W@C$_4$N$_4$ in distal pathway. In alternating pathway as shown in Fig. S3(b), *NHNH, *NHNH$_2$ and *NH$_2$NH$_2$ are generated sequentially and in these three hydrogenation steps, the ΔG of them are 0.31 eV, −0.40 eV and 0.54 eV. In the next steps, a pair of proton and electron continues to attack the distal nitrogen atom resulting that the first NH$_3$ molecule is released with the largely reduce of Gibbs free energy of −2.31 eV. Finally, the remaining NH$_3$ is also released with the ΔG of 0.53 eV. Although the PDS along the two pathways are different, the difference of limiting potential is only 0.1 V, and the NRR processes are supposed to perform in both two pathways for W@C$_4$N$_4$. For Re@C$_4$N$_4$ in vacuum, it has a very low change of ΔG in the first step (0.22 eV) and last step (0.17 eV), and the NRR path way of Re@C$_4$N$_4$ is discussed in Fig. 3

(c). In distal pathway, the four hydrogenation steps in intermediate process get the ΔG of 0.18 eV, −1.30 eV, 0.40 eV and −0.72 eV. The four-step Gibbs free energy changes in the alternating pathway are 0.76 eV, −0.36 eV, 0.15 eV and −2.00 eV as shown in Fig. S3(c). In the distal pathway, $U_L = -0.40$ V getting better performance than $U_L = -0.76$ V in alternating pathway, and the NRR process is inclined to complete the NRR reaction in distal pathway. The solvent effect on the NRR process is evaluated by the implicit solvation model performed in the VASPsol. As shown in Fig. 3(a-c), the ΔG in distal pathways of Mo@C$_4$N$_4$, W@C$_4$N$_4$ and Re@C$_4$N$_4$ are calculated. The U_L of Mo@C$_4$N$_4$, W@C$_4$N$_4$ and Re@C$_4$N$_4$ become −0.56 V, −0.29 V and −0.55 under the effect of implicit solvation model. Compare with vacuum environment, the U_L of Mo@C$_4$N$_4$ and Re@C$_4$N$_4$ increase, which shows that their catalytic activity will be weakened in solvent effect. Meanwhile, the U_L of W@C$_4$N$_4$ decrease, which illustrates that W@C$_4$N$_4$ is well suited to act as NRR catalysts in solvents. Compare the ΔG curves in vacuum and solvation model of Mo@C$_4$N$_4$, W@C$_4$N$_4$ and Re@C$_4$N$_4$, when the substrates have not released first NH$_3$, the solvation model has little effect on the ΔG of the systems. When adsorbed molecules get smaller during NRR process, the solvent effect will become more important.

Under acidic conditions, the required proton during the NRR process is supplied by the solution, so that the hydrogen evolution reaction (HER) is an important competition process of NRR. An efficient NRR catalyst should have good selectivity, and the performance of HER for Mo@C$_4$N$_4$, W@C$_4$N$_4$ and Re@C$_4$N$_4$ is evaluated to reveal the realistic NRR activity as Fig. 3(d). The Gibbs free energy decrease when proton bonds with the metal atom due to a strong interaction between them, and the limiting potentials of HER are −0.36 V, −0.74 V and −0.57 V for Mo@C$_4$N$_4$, W@C$_4$N$_4$ and Re@C$_4$N$_4$. It is observed that Mo@C$_4$N$_4$ has the lowest limiting potential for HER, and thus HER process is very effortless to occur.

The W@C$_4$N$_4$ has the highest limiting potential for HER, which makes HER process hard to take place. In particular, the limiting potential for HER of Re@C$_4$N$_4$ is moderate, which means that the difficulty of HER reaction for Re@C$_4$N$_4$ is between Mo@C$_4$N$_4$ and W@C$_4$N$_4$. To be clear, when the limiting potential of NRR is significantly lower than HER, the catalyst can effectively inhibit the competitive hydrogen evolution reaction. Compared to the limiting potential of NRR and HER, the Mo@C$_4$N$_4$ is preferred to the HER process, and W@C$_4$N$_4$ and Re@C$_4$N$_4$ are preferred to the NRR process. So far, the W@C$_4$N$_4$ and Re@C$_4$N$_4$ exhibit the promising NRR catalytic activity and selectivity. In addition, in order to further confirm the stability of the catalyst after the screening, the thermodynamic stability of W@C$_4$N$_4$ and Re@C$_4$N$_4$ are acquired by molecular dynamic (MD) calculation in 300 K, 400 K and 500 K as shown in Fig. S4. The energy curve fluctuates very little at different temperatures, and the structures of the catalyst remain almost unchanged. It is demonstrated that W@C$_4$N$_4$ and Re@C$_4$N$_4$ have both high NRR catalytic activity and high structural stability, which are perfect to reduce nitrogen.

3.4. Origin of NRR activity on W@C$_4$N$_4$ and Re@C$_4$N$_4$

To further reveal the mechanism behind the high NRR activity of W@C$_4$N$_4$ and Re@C$_4$N$_4$, the difference of charge density, DOS and COHP are investigated. The differential charge density of W@C$_4$N$_4$ and Re@C$_4$N$_4$ during the nitrogen adsorbed on the sub-

strate is shown in Fig. 4(a). The blue areas express the dissipation of electrons, and the yellow areas express the aggregation of electrons. For W@C$_4$N$_4$, it can be clearly noticed that the electron depletion appears near the two N atoms, meanwhile the area between the TM atom and closed N atom occurs electron accumulation which indicates the chemical bonds are formed by the donation process. Briefly, the empty d orbital of the metal accepts the nitrogen's electrons and forms chemical bonds. what's more, the electron accumulation occurs near two N atoms indicating that electron backdonation. And the similar pattern emerges in Re@C$_4$N$_4$, by Bander charge analysis, the 0.32 e of electrons are transferred to the nitrogen molecule from W atom, and there are also 0.29 e of electrons transferred from Re atom to nitrogen molecule. To explore the changes of orbitals for nitrogen molecule and TM atom after adsorption, the DOS is calculated. The DOS of nitrogen molecule before adsorption is shown in Fig. 4(b). For the free nitrogen molecule, σ, σ^* and π orbitals locate below the Fermi level, and the π^* antibonding orbitals locate so much higher above the Fermi level, which leads to the high stability of nitrogen molecules. After the nitrogen molecule adsorbed on the W@C$_4$N$_4$ and Re@C$_4$N$_4$, the PDOS including the nitrogen molecule and TM atoms (W or Re) are shown in Fig. 4(c) and 4(d). For W@C$_4$N$_4$, obviously, the appearance of many hybridized peaks indicates that nitrogen molecular orbitals are strongly hybridized with the metal orbitals because d orbitals of the metal atom are near or upper the Fermi level, where approach the π^* antibonding orbitals. After hybridization between
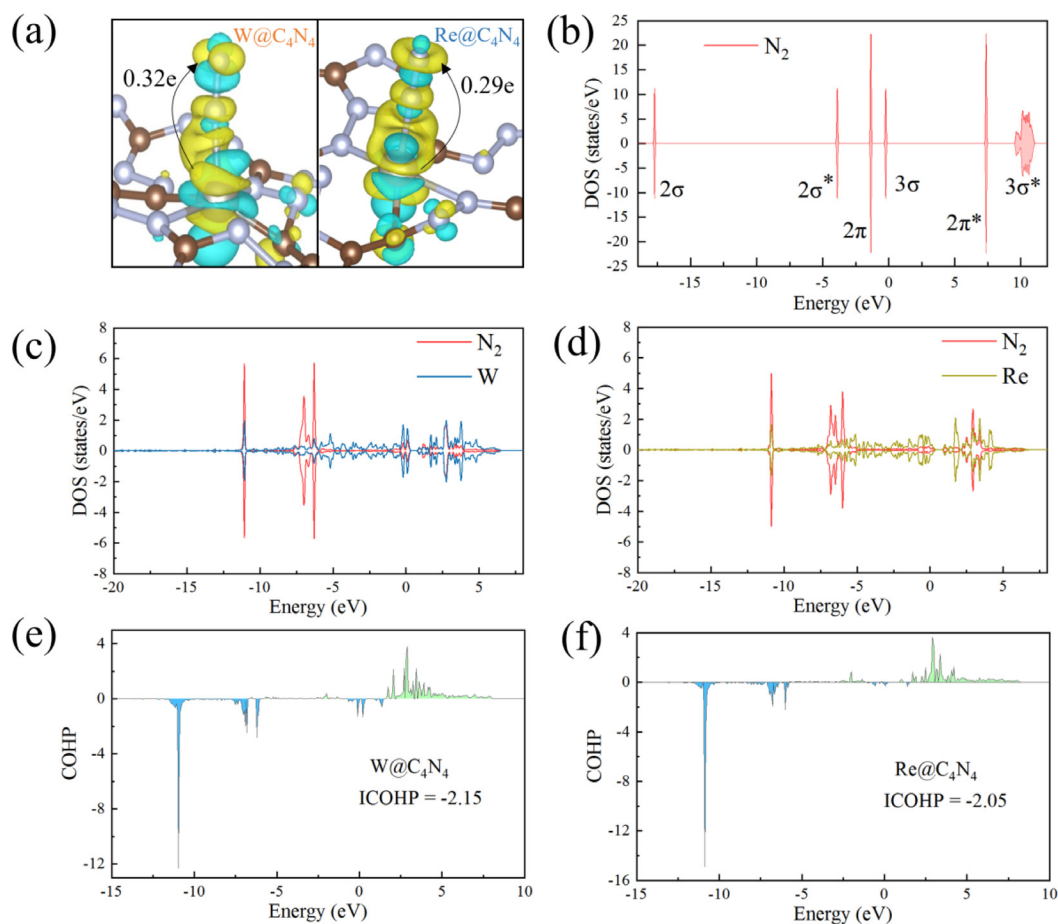

Fig. 4. (a) Charge density difference after N$_2$ adsorption on W@C$_4$N$_4$ and Re@C$_4$N$_4$ (Cyan and yellow respectively represent the consumption and accumulation of electrons. The isosurface value is set to 0.0035 e Å^{-3}). (b) The density of states (DOS) of free N$_2$ molecule. (c) The partial density of states (PDOS) of the adsorbed N$_2$ molecule on W@C$_4$N$_4$ and the W atom binding to the N$_2$. (d) The PDOS of the adsorbed N$_2$ molecule on Re@C$_4$N$_4$ and the Re atom binding to the N$_2$. The Fermi level in DOS and COHP figures is set to 0 eV. (e) The crystal orbital Hamilton population (COHP) between W atom binding to N$_2$ and N atom of N$_2$ in W@C$_4$N$_4$. (f) The COHP between Re atom binding to N$_2$ and N atom of N$_2$ in Re@C$_4$N$_4$.

orbitals of the metal atom and π^* antibonding orbitals of nitrogen molecule, the π^* orbitals are shifted left below the Fermi level partial. In this case, π^* antibonding orbital can be filled, which weakens the N≡N bonds and makes subsequent hydrogenation steps carry out. Re@C$_4$N$_4$ exhibits very similar performance. The strong hybridization below the Fermi level represents the transfer of electrons from nitrogen to empty metal orbitals in donation process, which result in dramatic change of the PDOS of nitrogen molecule and also describe a strong binding between the N and Re atoms. On the other hand, the hybridization above and around Fermi level represents the backdonation process, in which the electrons are transferred from Re atoms to nitrogen molecules. In order to further study the bonding property of nitrogen molecules and metal atoms, as shown in Fig. 4(e and f), the COHP and the ICOHP between N and TM atoms of W@C$_4$N$_4$ and Re@C$_4$N$_4$ are computed. The ICOHP of the adsorption configuration of W@C$_4$N$_4$ is −2.15, and the value of Re@C$_4$N$_4$ is −2.05. The two large negative values demonstrate a very strong bond between the metal atom and nitrogen atom. The peaks with positive COHP values above the Fermi level represent the subsistent of backdonation mechanism, the electrons are shifted from the metal d orbitals to the nitrogen π^* antibonding orbital. With regard to the electronic structures, the W@C$_4$N$_4$ and Re@C$_4$N$_4$ get high activity for NRR process because the W and Re atoms have the appropriate amount of unoccupied d orbitals and valence electron, and these build the balance between adsorption and activation for nitrogen molecules.

To study the specific role of each part of catalyst in the NRR process, understand the transfer of electron in the system, the distribution diagram of charge for W@C$_4$N$_4$ and Re@C$_4$N$_4$ are obtained by Bander charge analysis. As shown in Fig. 5(a), the adsorption structures during the NRR process are separated into three parts. The moiety 1 is N$_x$H$_y$, which represents the intermediates formed by hydrogenation of nitrogen during the NRR reaction. The moiety 2 is composed of metal atom and its coordination atoms. In W@C$_4$N$_4$ and Re@C$_4$N$_4$, the coordination atoms are two carbon atoms and two nitrogen atoms. The moiety 3 is the substrate without other moieties. As shown in Fig. 5(b), the first step of reaction

pathway represents that nitrogen is adsorbed on W atom. The next six steps are the hydrogenation steps of nitrogen. In the first step, electrons from the moiety 2 are transferred to the substrate and N$_2$. Before the first NH$_3$ molecule is released, more and more electrons are transferred from the moiety 2 to N$_x$H$_y$. With the formation of *N species, moiety 1 gets the most electrons during NRR process. Then hydrogenation continues, the electrons of N$_x$H$_y$ transfer back to the moiety 2. The intermediates get a lower electron requirement probably because there is only one nitrogen atom left, and the nitrogen atom becomes gradually saturated for linking more hydrogen atoms. As shown in Fig. 5(c), the charge distribution of Re@C$_4$N$_4$ exhibits the very similar performance. In the whole NRR process, the distribution trend of charge in moiety 1 and moiety 2 are nearly opposite, which indicates that the N$_x$H$_y$ exchanges electrons directly with metal atom. The substrate serves as a huge source of electron to balance the charge distribution of other moieties.

3.5. New descriptor φ via exploring the intrinsic properties of metal atoms

In the study of TM@C$_4$N$_4$ as high-performance NRR catalysts, the traditional multi-step screening method is used, which includes adsorption free energy and changes in the bond length of nitrogen molecules, the ΔG in the first and last step of hydrogenation process and the U_L by calculating the entire pathways of NRR. There is no doubt that multi-step screening method consumes much time and resources. Fortunately, a number of descriptors have been found to describe high-performance NRR catalysts [61,62]. However, there are still many shortcomings, and many properties involved in the descriptors such as charge transfer and change of Gibbs energy are obtained with calculation. Using the intrinsic properties of materials as descriptors can greatly speed up the screening process of NRR catalysts. Here, SISSO package is used to identify a descriptor φ, which is used to describe the activation of NRR process for TM@C$_4$N$_4$. In previous studies, N≡N bond length in the adsorption process has been proven to be an effective
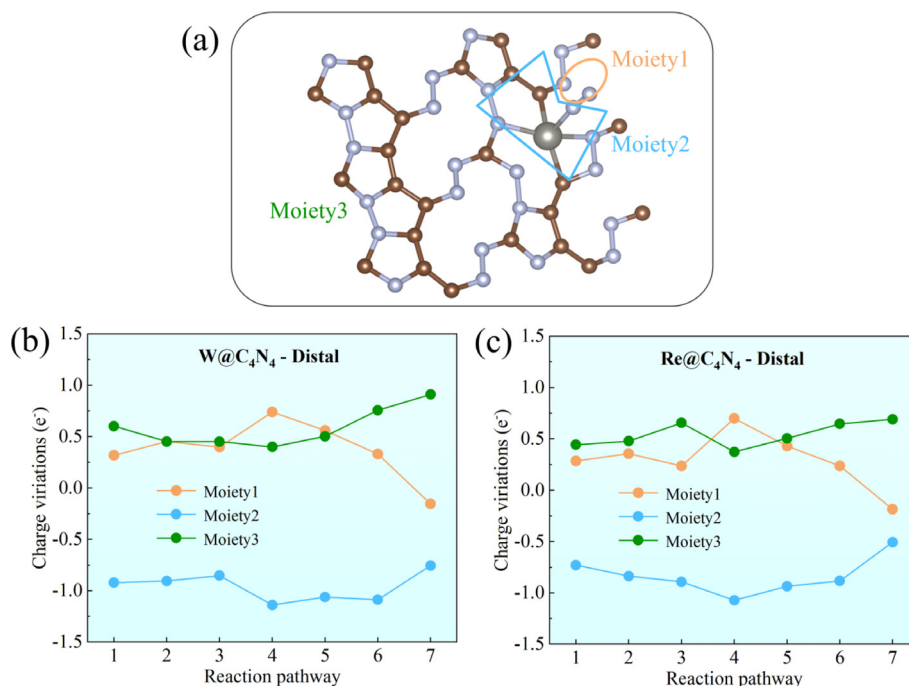

Fig. 5. (a) Diagram of the division of three moieties in W@C$_4$N$_4$ and Re@C$_4$N$_4$. (b) Schematic diagram of three moieties and charge variation of the NRR on W@C$_4$N$_4$. (c) Schematic diagram of three moieties and charge variation of the NRR on Re@C$_4$N$_4$.
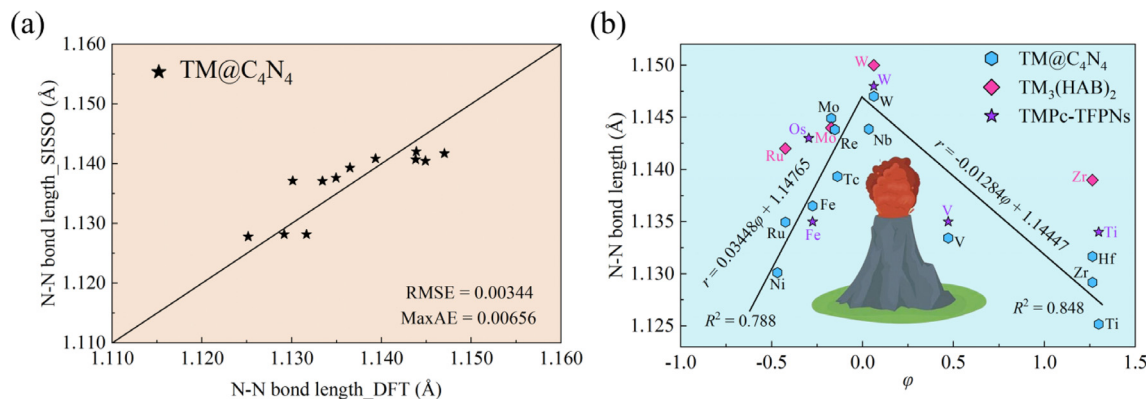
Fig. 6. (a) Comparison N≡N bond length between SISSO and DFT. (b) The 'volcano' relationship between N≡N bond length and φ in TM@C$_4$N$_4$, TM$_3$(HAB)$_2$, and TMPc-TFPNs.

descriptor of NRR process [63]. Herein, the N≡N bond length calculated by DFT and Predicted by SISSO are compared as shown in Fig. 6(a). It can be seen that the trend predicted by the N≡N bond length of SISSO on the catalyst adsorption process is roughly the same as that calculated by the DFT method. Then the best-performing one-dimensional descriptor φ in SISSO is selected. The descriptor φ is correlated with N≡N bond length to measure NRR activity for TM@C$_4$N$_4$ (TM = Ti, V, Fe, Ni, Zr, Nb, Mo, Tc, Ru, Hf, W, Re) with end-on configuration, and it is defined as m/n - b/l. Here, m is the number of empty d orbitals in the free metal atom, n is the number of electrons that the free metal d orbital has filled, b is the covalent radius represents that half of the distance of two atoms, and these atoms are bonded with a single covalent bond for their typical oxidation number and coordination, and l is the atomic radius (non-bonded) of metal atom which means that half of the distance of two unbonded atoms. The two atoms are the same element, and the electrostatic forces are balanced. The 'volcano' relationship between N≡N bond length in adsorption process and descriptor φ is constructed as shown in Fig. 6(b). It can be found that when φ is close to 0, the N≡N bond length reaches its maximum value, which means that the catalysts have the highest catalytic activity simultaneously. More importantly, the catalysts screened by DFT calculation has a lower limiting potential such as Re@C$_4$N$_4$ and W@C$_4$N$_4$, and they have the larger N≡N bond length when their φ value is close to 0. The descriptor φ of other NRR catalysts is also researched, and the same pattern is observed in catalysts such as TMPc-TFPNs [64] and TM$_3$(HAB)$_2$ [65], which prove that this descriptor is universal to many systems. Subsequently, the mechanism behind the descriptor φ is further discussed.

When φ value is close to 0, the value of m/n is close to b/l. Here, m/n is the number of empty d orbitals divided by number of electrons that the free metal d orbital has filled. If the metal atom has only one electron in its outer orbital, this orbital is going to be seen as a half-full orbital with the value of 0.5. The value of m/n is regarded as an intrinsic property of a metal atom. The b/l is viewed as a variable value with coordination environment. Many studies have demonstrated the ability of various metals to perform the NRR process. However, only a few metals have high NRR activity on a specific substrate. The descriptor φ leads to an answer that most metal atoms possess potential NRR activity, and the potential NRR activity of metal atoms can only be realized if the surrounding substrate environment is suitable for metal atoms. This provides a new way to study NRR catalyst that calculating the intrinsic properties of a particular atom, and looking for different substrates to match different values of b/l.

4. Conclusions

In this study, the TM@C$_4$N$_4$ as the efficient catalysts for NRR is examined, and TM@C$_4$N$_4$ has extremely high structural stability as SACs. For the doped 29 TM@C$_4$N$_4$ structures, through the multi-step screening method by calculating the N$_2$ adsorption and activation, reaction mechanism of NRR process and selectivity between HER and NRR, W@C$_4$N$_4$ and Re@C$_4$N$_4$ are selected as high activity NRR catalysts with limiting potentials of −0.29 V and −0.55 V. Differential charge density, density of states, crystal orbital Hamilton population and charge transfer are used to reveal the NRR activity source of W@C$_4$N$_4$ and Re@C$_4$N$_4$. Furthermore, the descriptor φ (m/n - b/l) is obtained by SISSO method, and the "volcano" relationship between descriptor φ and N≡N bond length in adsorption process is constructed. The descriptor φ can not only effectively describe the catalytic activity of SACs, but also provides a new strategy for designing NRR catalysts. In general, this work screens TM@C$_4$N$_4$ for the high catalytic activity of NRR, and provides a new way to design High performance SACs.

Declaration of competing interest

The authors declare that they have no known competing financial interests or personal relationships that could have appeared to influence the work reported in this paper.

Appendix A. Supplementary material

Supplementary data to this article can be found online at https://doi.org/10.1016/j.jechem.2023.05.022.

References

[1] R. Poudyal, P. Loskot, R. Nepal, R. Parajuli, S.K. Khadka, Renew. Sust. Energ. Rev. 116 (2019).

[2] J.W. Makepeace, T. He, C. Weidenthaler, T.R. Jensen, F. Chang, T. Vegge, P. Ngene, Y. Kojima, P.E. de Jongh, P. Chen, W.I.F. David, Int. J. Hydrog. Energy 44 (2019) 7746–7767.

[3] T. Zhang, J. Uratani, Y. Huang, L. Xu, S. Griffiths, Y. Ding, Renew. Sust. Energ. Rev. 176 (2023).
[4] L. Niu, L. An, X. Wang, Z. Sun, J. Energy Chem. 61 (2021) 304–318.
[5] Z. Huang, M. Rafiq, A.R. Woldu, Q.-X. Tong, D. Astruc, L. Hu, Coord. Chem. Rev. 478 (2023).
[6] B.H.R. Suryanto, H.-L. Du, D. Wang, J. Chen, A.N. Simonov, D.R. MacFarlane, Nat. Catal. 2 (2019) 290–296.
[7] F. Li, Q. Tang, Nanoscale 11 (2019) 18769–18778.
[8] D. Han, X. Liu, J. Cai, Y. Xie, S. Niu, S. Wu, Y. Zang, Y. Fang, F. Zhao, W. Qu, M. Chen, G. Wang, Y. Qian, J. Energy Chem. 59 (2021) 55–62.
[9] K. Chu, Y.-P. Liu, Y.-B. Li, J. Wang, H. Zhang, ACS Appl. Mater. Interfaces 11 (2019) (1815) 31806–131803.
[10] H. Liu, Chin. J. Catal. 35 (2014) 1619–1640.
[11] L. Ma, F. Xu, L. Zhang, Z. Nie, K. Xia, M. Guo, M. Li, X. Ding, J. Energy Chem. 71 (2022) 182–187.
[12] H. Zhong, M. Wang, M. Ghorbani-Asl, J. Zhang, K.H. Ly, Z. Liao, G. Chen, Y. Wei, B.P. Biswal, E. Zschech, I.M. Weidinger, A.V. Krasheninnikov, R. Dong, X. Feng, J. Am. Chem. Soc. 143 (2021) 19992–20000.
[13] K. Chu, W. Gu, Q. Li, Y. Liu, Y. Tian, W. Liu, J. Energy Chem. 53 (2021) 82–89.
[14] Z. Xue, X. Zhang, J. Qin, R. Liu, J. Energy Chem. 57 (2021) 443–450.
[15] Y. Yang, Y. Yang, Z. Pei, K.-H. Wu, C. Tan, H. Wang, L. Wei, A. Mahmood, C. Yan, J. Dong, S. Zhao, Y. Chen, Matter 3 (2020) 1442–1476.
[16] P. Yi, L. Bingzhang, C. Shaowei, Adv. Mater. 30 (2018) 1801995.
[17] K. Ohashi, K. Iwase, T. Harada, S. Nakanishi, K. Kamiya, J. Phys. Chem. C 125 (2021) 10983–10990.
[18] X. Wan, W. Chen, J. Yang, M. Liu, X. Liu, J. Shui, ChemElectroChem 6 (2019) 304–315.
[19] C. Ling, X. Niu, Q. Li, A. Du, J. Wang, J. Am. Chem. Soc. 140 (2018) 14161–14168.
[20] T. Yang, T.T. Song, J. Zhou, S. Wang, D. Chi, L. Shen, M. Yang, Y.P. Feng, Nano Energy 68 (2020).
[21] Y. Yue, Y. Chen, X. Zhang, J. Qin, X. Zhang, R. Liu, Appl. Surf. Sci. 606 (2022).
[22] T. Liu, Q. Dang, X. Zhou, J. Li, Z. Ge, H. Che, S. Tang, Y. Luo, J. Jiang, Chem.-Eur. J. 27 (2021) 6945–6953.
[23] Y. Kong, D. Liu, H. Ai, K.H. Lo, S. Wang, H. Pan, ACS Appl. Nano Mater. 3 (2020) 11274–11281.
[24] B. Mohanty, S. Basu, B.K. Jena, J. Energy Chem. 70 (2022) 444–471.
[25] L. Shi, Y. Yin, S. Wang, H. Sun, ACS Catal. 10 (2020) 6870–6899.
[26] M. Arif, M. Babar, U. Azhar, M. Sagir, M. Bilal Tahir, M. Asim Mushtaq, G. Yasin, M. Mubashir, J. Wei Roy Chong, K. Shiong Khoo, P. Loke Show, Chem. Eng. J. 451 (2023).
[27] X. Kang, J. Huang, X. Duan, Phys. Chem. Chem. Phys. 24 (2022) 17155–17162.
[28] Y. Zhang, N. Ma, Y. Wang, B. Liang, J. Fan, Appl. Surf. Sci. 623 (2023).
[29] H. Chai, W. Chen, Z. Feng, Y. Li, M. Zhao, J. Shi, Y. Tang, X. Dai, Nanomaterials 13 (2023) 1433.
[30] A. Banerjee, Catal. Today 418 (2023).
[31] Q. Zhang, X. Wang, F. Zhang, C. Fang, D. Liu, Q. Zhou, ACS Appl. Mater. Interfaces 15 (2023) 11812–111811.
[32] W. Dong, X. Chen, J. Peng, W. Liu, X. Jin, G. Ni, Z. Liu, Chem. Res. Chin. Univ. 36 (2020) 648–661.
[33] D. Chen, Z. Chen, L. Chen, Y. Li, S. Xiao, B. Xiao, J. Colloid Interface Sci. 607 (2022) 1551–1561.
[34] H. Jin, C. Guo, X. Liu, J. Liu, A. Vasileff, Y. Jiao, Y. Zheng, S.-Z. Qiao, Chem. Rev. 118 (2018) 6337–6408.
[35] M.K. Lee, M. Shokouhimehr, S.Y. Kim, H.W. Jang, Adv. Energy Mater. 12 (2022) 2003990.
[36] X. Zhai, L. Li, X. Liu, Y. Li, J. Yang, D. Yang, J. Zhang, H. Yan, G. Ge, Nanoscale 12 (2020) 10035–10043.
[37] K. Liu, J. Fu, L. Zhu, X. Zhang, H. Li, H. Liu, J. Hu, M. Liu, Nanoscale 12 (2020) 4903–4908.
[38] W. Yang, H. Huang, X. Ding, Z. Ding, C. Wu, I.D. Gates, Z. Gao, Electrochim. Acta 335 (2020).
[39] M. Yan, L.J. Arachchige, A. Dong, X.L. Zhang, Z. Dai, C. Sun, Inorg. Chem. 60 (2021) 18314–18324.
[40] F. Wang, J. Mao, Diam. Relat. Mat. 118 (2021).
[41] Y. Liu, B. Song, C.-X. Huang, L.-M. Yang, J. Mater. Chem. A 10 (2022) 13527–13543.
[42] Z. Zhao, Y. Long, S. Luo, Y. Luo, M. Chen, J. Ma, J. Energy Chem. 60 (2021) 546–555.
[43] N. Zhang, Y. Gao, L. Ma, Y. Wang, L. Huang, B. Wei, Y. Xue, H. Zhu, R. Jiang, Int. J. Hydrog. Energy 48 (2023) 7621–7631.
[44] Z. Wei, J. He, Y. Yang, Z. Xia, Y. Feng, J. Ma, J. Energy Chem. 53 (2021) 303–308.
[45] Y. Chen, M. Zhao, Z. Wang, Q. Jiang, ChemPhysChem (2023) e202300012.
[46] Y. Wang, J. Lv, L. Zhu, Y. Ma, Comput. Phys. Commun. 183 (2012) 2063–2070.
[47] R. Ouyang, S. Curtarolo, E. Ahmetcik, M. Scheffler, L.M. Ghiringhelli, Phys. Rev. Mater. 2 (2018).
[48] G. Kresse, J. Furthmuller, Phys. Rev. B 54 (1996) 11169–11186.
[49] G. Kresse, D. Joubert, Phys. Rev. B 59 (1999) 1758–1775.
[50] J.P. Perdew, K. Burke, M. Ernzerhof, Phys. Rev. Lett. 77 (1996) 3865–3868.
[51] M. Ernzerhof, G.E. Scuseria, J. Chem. Phys. 110 (1999) 5029–5036.
[52] P.E. Blochl, Phys. Rev. B 50 (1994) 17953–17979.
[53] L.A. Burns, A. Vazquez-Mayagoitia, B.G. Sumpter, C.D. Sherrill, J. Chem. Phys. 134 (2011).
[54] K. Mathew, V.S.C. Kolluru, S. Mula, S.N. Steinmann, R.G. Hennig, J. Chem. Phys. 151 (2019).
[55] K. Mathew, R. Sundararaman, K. Letchworth-Weaver, T.A. Arias, R.G. Hennig, J. Chem. Phys. 140 (2014).
[56] B. Huang, Y. Wu, B. Chen, Y. Qian, N. Zhou, N. Li, Chin. J. Catal. 42 (2021) 1160–1167.
[57] W. Song, K. Xie, J. Wang, Y. Guo, C. He, L. Fu, Phys. Chem. Chem. Phys. 23 (2021) 10418–10428.
[58] Y. Wu, C. He, W. Zhang, J. Am. Chem. Soc. 144 (2022) 9344–9353.
[59] C. He, C. Xu, W. Zhang, Appl. Surf. Sci. 606 (2022).
[60] J. Wu, L. Yu, S. Liu, Q. Huang, S. Jiang, A. Matveev, L. Wang, E. Song, B. Xiao, J. Inorg. Mater. 37 (2022) 1141–1148.
[61] T. Deng, C. Cen, H. Shen, S. Wang, J. Guo, S. Cai, M. Deng, J. Phys. Chem. Lett. 11 (2020) 6320–6329.
[62] J. Qi, S. Zhou, K. Xie, S. Lin, J. Energy Chem. 60 (2021) 249–258.
[63] F. Liu, L. Song, Y. Liu, F. Zheng, L. Wang, K. Palotas, H. Lin, Y. Li, J. Mater. Chem. A 8 (2020) 3598–3605.
[64] J. Wang, Z. Zhang, Y. Li, Y. Qu, Y. Li, W. Li, M. Zhao, ACS Appl. Mater. Interfaces 14 (2022) 1024–1033.
[65] M.-R. Zhao, B. Song, L.-M. Yang, ACS Appl. Mater. Interfaces 13 (2021) 26109–26122.